International Journal of Minerals, Metallurgy and Materials
Volume 28, Number 11, November 2021, Page 1788
https://doi.org/10.1007/s12613-020-2089-x

Shape of slab solidification end under non-uniform cooling and its influence on the central segregation with mechanical soft reduction

Jie Li[1,3], *Yan-hui Sun*[1], *Hang-hang An*[1], *and Pei-yuan Ni*[2]

1) Collaborative Innovation Center of Steel Technology, University of Science and Technology Beijing, Beijing 100083, China
2) School of Metallurgy, Northeastern University, Shenyang 110819, China
3) Hesteel Group Technology Research Institute, Shijiazhuang 050000, China
(Received: 25 March 2020; revised: 3 May 2020; accepted: 6 May 2020)

Abstract: In order to study the effect of continuous casting process parameters on the shape of slab solidification end under non-uniform cooling, a solidification model of a continuous-cast slab with non-uniform cooling condition was established with ProCAST software. The model was verified by the results of nail shooting tests and the infrared temperature measurement equipment. Four characteristic parameters were defined to evaluate the uniformity of the shape of slab solidification end. The results showed that the nonuniformity at the beginning and end of solidification, the solidification end length, and the solidification unevenness increased with the rise of casting speed. For each 10°C increase of superheat, the solidification unevenness increased by about 0.022. However, the effect of superheat on the solidification end length can be ignored. The secondary cooling strength showed minimal effect on the nonuniformity at the beginning and end of solidification. With the increase in secondary cooling intensity, the solidification end length decreased, but the solidification unevenness increased. In addition, the central segregation of the slab produced with and without the mechanical soft reduction (MSR) process was investigated. The transverse flow of molten steel with low solid fraction influenced the central segregation morphology under MSR.

Keywords: continuous casting; heat transfer model; nail shooting; shape of solidification end; central segregation

1. Introduction

Macrosegregation is an important topic in engineering [1–2]. Central segregation of slab affects the evenness of the final steel structure. Segregation primarily results in a banded structure formation that affects the product performance [3–5]. Therefore, the control of central segregation has been a concern among metallurgists. Electromagnetic stirring and mechanical soft reduction (MSR) are important techniques that are used to decrease central segregation in continuous-cast slabs. Thermal soft reduction (TSR) is an additional technique used in continuous-cast slab to reduce central segregation [6].

MSR is an effective method to control central segregation; it has been developed rapidly in the past decades [7–12]. The optimum zone for improving internal structure is defined by a minimum reduction, which is necessary to compensate for the shrinkage during solidification to avoid internal cracks [13]. However, the optimum process parameters for MSR remain in the trial stage in plant operations. Yim *et al*. [14] considered the appropriate MSR zone to be a central solid fraction f_s = 0.40–0.80. Finland Rautaruukki believed that the optimal MSR zone for the production of low alloyed steel of 210 mm × (1250–1475) mm slab caster is f_s = 0.30–0.90 [15]. Ji *et al*. [16] suggested that the MSR parameters of peritectic steel should be selected as f_s = 0.60–0.90 in continuous-cast slab process. Ito *et al*. [17] studied and obtained a regression equation to estimate the internal reduction efficiency. Wu *et al*. [18] pointed out that the theory of MSR technology had not been formed and studied the principle of MSR in slab casting. Different from square billets, a problem of non-uniform cooling exists in the transverse direction of slabs. The predecessors' views on the optimal MSR zone of slabs are inconsistent, and this condition maybe largely related to the solidification end morphology of slabs.

The formation mechanism of central segregation in continuous-cast slabs has been studied by researchers. Domitner *et al.* [19] developed a full-scale model to investigate the macrosegregation formation in continuous-cast of a binary Fe–C alloy. Rogberg and Ek [20] developed a mathematical

Corresponding author: Yan-hui Sun E-mail: sunyanhui@metall.ustb.edu.cn

model to calculate the liquid flow velocity along the strand with MSR.

The shell thickness of a continuous-cast slab is non-uniform during solidification [21–22]. In the production of wide and thick slabs, most steel plants shut down the edge nozzles and reduce the cooling intensity to avoid edge and corner cracks caused by undercooling of several low alloyed steel slabs; this step can effectively increase the corner temperature and reduce corner cracks. However, uneven cooling affects the heat transfer and shape of solidification end in the slab, resulting in unsatisfactory MSR process. Ji *et al.* [16] developed a two-dimensional heat transfer model to analyze uneven solidification, particularly in the shape of slab solidification end. Long *et al.* [23] investigated the effect of uneven solidification on steel quality while considering the realistic cooling intensity along all directions. The segregation degree in the width direction of the slab was different [24–25]. With additional strict requirements of customers for steel quality, the problem of uneven cooling of slabs in the transverse direction will be given more attention.

In the present study, the solidification and heat transfer model of a wide slab was established to investigate the influences of continuous casting process parameters on the shape of the solidification end. In addition, the effect of the shape of slab solidification end on the central segregation of slab was investigated during MSR.

2. Heat transfer and solidification model of wide slab

2.1. Governing equation and material properties

2.1.1. Governing equation

According to Fourier's and energy conservation laws, the solidification heat transfer process of continuous-cast slab is a three-dimensional heat transfer process, and its heat transfer equation can be expressed by Eq. (1):

$$\rho(T)c(T)\frac{\partial T}{\partial t}-\left[\frac{\partial T}{\partial x}\left(k(T)\frac{\partial T}{\partial x}\right)+\frac{\partial T}{\partial y}\left(k(T)\frac{\partial T}{\partial y}\right)+\frac{\partial T}{\partial z}\left(k(T)\frac{\partial T}{\partial z}\right)\right]=0 \quad (1)$$

where T is the temperature, °C; t is the solidification time, s; $k(T)$ is the thermal conductivity, $W\cdot m^{-1}\cdot K^{-1}$; $\rho(T)$ is the density of steel, kg/m^3; $c(T)$ is the real specific heat, $J\cdot kg^{-1}\cdot °C^{-1}$.

2.1.2. Material properties

SA516Gr70 grade steel was selected as the test material, and its nominal composition is shown in Table 1. Accurate material properties are essential for numerical simulation. In this study, the thermal conductivity, density, heat transfer, and solid fraction of simulated steel grades were calculated by using the thermodynamic database of ProCAST software (Fig. 1).

Table 1. Nominal Composition of SA516Gr70 wt%

C	Si	Mn	P	S	Nb	Al	Ca	Fe
0.17	0.25	1.15	0.0080	0.0015	0.0170	0.025	0.0015	Bal.

2.2. Geometric model and boundary conditions

2.2.1. Geometric model

In the present study, a straight-arc type caster with a section size of 200 mm × 2300 mm was selected as the research object. Table 2 shows the main technical parameters of the caster.

The "slicing method" was used to simulate the solidification process of slab to reduce calculations. A geometric model with 200 mm × 1150 mm × 15 mm dimensions was constructed and meshed as shown in Fig. 2. A total of 64504 elements and 14469 nodes were obtained.

2.2.2. Boundary conditions in the casting mold

The solidification behavior of the slab in the mold is very important for the surface quality of the slab [26]. The surface temperature change of a slab in mold is complicated. The heat flux at the slab boundary can be assumed to be independent of temperature. In this study, the boundary conditions in the casting mold were simplified, and the heat flux can be calculated from Eq. (2), which was proposed by Savage and Pritchard [27]:

$$q_m = A - B\sqrt{t} \quad (2)$$

where q_m is the heat flux of the mold, W/m^2; A and B are the coefficients depending on the mold cooling conditions; t is the time in the mold, s. In this study, A is 2.68×10^6, and B was optimized based on the actual situation.

2.2.3. Boundary conditions at secondary cooling zone

Continuous-cast slab was drawn out from the mold to the secondary cooling zone. In this area, aside from radiation to the surrounding area and conduction of heat removal through the supporting roll, the primary means of heat dissipation was from surface cooling by spraying water. Heat flux was calculated as follows [28]:

$$q_s = h_w(T_s - T_w) + h_r(T_s - T_r) + q_{rad} \quad (3)$$

where q_s is the heat flux of the secondary cooling zone, W/m^2; h_w is the heat transfer coefficient of cooling spray, $W\cdot m^{-2}\cdot K^{-1}$; T_s is the surface temperature, °C; T_w is the water temperature, °C; h_r is the effective heat transfer coefficient between the rolls and slab, $W\cdot m^{-2}\cdot K^{-1}$; T_r is the roll temperature, °C; q_{rad} is the radiation heat flux, W/m^2.

In regions of secondary cooling spray, heat transfer coefficients were calculated using the formula of Nozaki *et al.* [29]:

$$h_w(x) = \frac{1570 w_x^{0.55}(1-0.0075T_w)}{\alpha} \quad (4)$$

where x is the position from center to corner of the slab surface; w_x is the spray-cooling flux at x, $L\cdot m^{-2}\cdot s^{-1}$; α is a machine-dependent calibration factor; $h_w(x)$ is the spray-cooling heat transfer coefficient at x, $kW\cdot m^{-2}\cdot K^{-1}$.

In the roll contact regions, the effective contact heat transfer

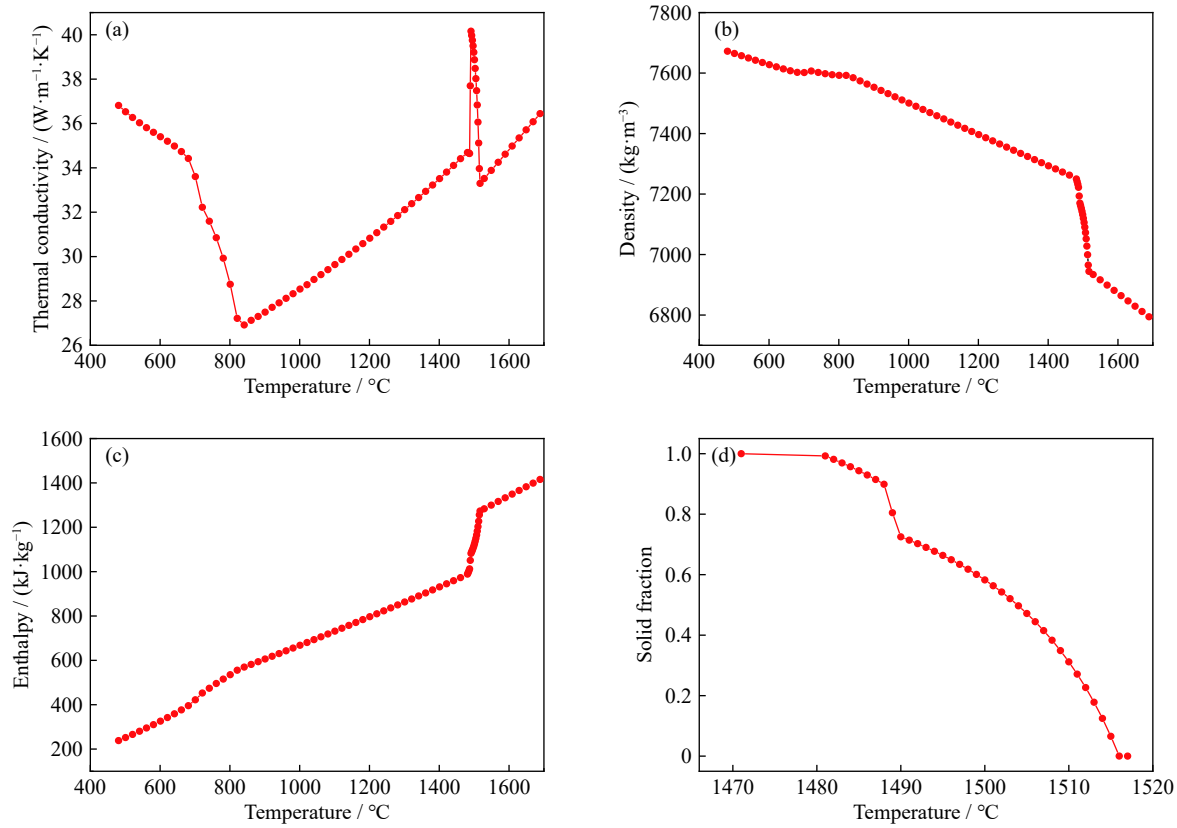

Fig. 1. Material properties of SA516Gr70: (a) thermal conductivity; (b) density; (c) enthalpy; (d) solid fraction.

Table 2. Main technical parameters of the caster

Caster type	Sectional dimension / (mm × mm)	Caster radius / m	Metallurgical length / m	Mold length / m	Cast speed range / (m·min^{-1})
Straight-arc	200 × 2300	10.5	35.8	0.90	0.5–1.5

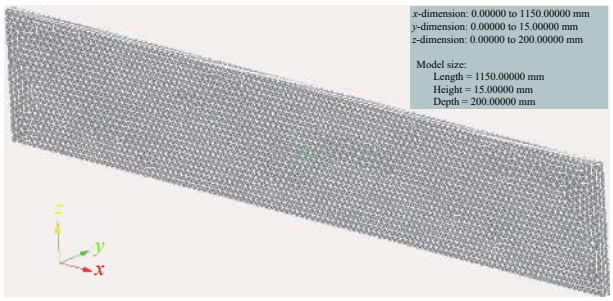

Fig. 2. Main view of geometric model after meshing.

coefficients between rolls and slab were calculated by the following formula:

$$h_r = N\frac{h_{r0}\cdot L_0}{L} \tag{5}$$

where h_{r0} is the heat transfer coefficient between the slab and roll, kW·m^{-2}·K^{-1}; L_0 is the contact length, m; N is the roller number; L is the length of cooling zone, m. In this study, L_0 = 5 mm, and h_{r0} = 2.5 kW·m^{-2}·K^{-1}, according to previous research [28,30].

In foot-roll and bending sections, no deliberate reduction of the edge nozzle and water volume was observed, and water distribution was uniform. The heat transfer coefficient on the width is equal. The number and quantity of nozzles at the edge of slab were reduced in segment 1 (Seg. 1) to Seg. 9, and the cooling intensity was reduced to obtain a high surface temperature. Fig. 3 shows the actual water distributions of Segs. 1–9.

2.2.4. Boundary conditions of radiation mathematical model

In several cooling zones, a part of the slab was not cooled by spray water. Thus, the heat extraction q_{rad} was calculated as follows:

$$q_{rad} = \varepsilon\sigma\left[(T_s+273)^4-(T_{amb}+273)^4\right] \tag{6}$$

where σ is Stefan–Boltzmann constant, 5.67×10^{-8} W·m^{-2}·K^{-4}; ε is steel emissivity; T_{amb} is the ambient temperature, °C.

The surface emissivity for steel was considered a function of surface temperature determined from the data compiled by Touloulian *et al.* [31]:

$$\varepsilon = \frac{0.85}{1+\exp\left[(42.68-0.02682(T_s+273)\right]^{0.0115}} \tag{7}$$

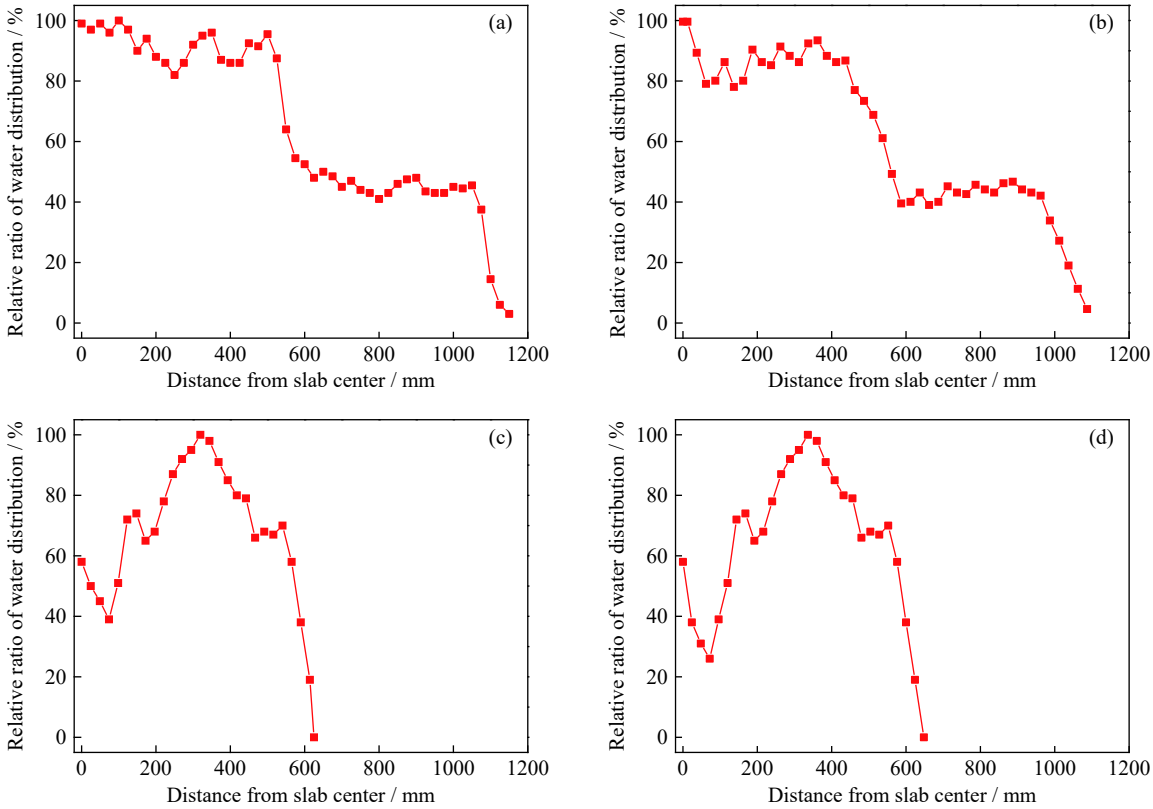

Fig. 3. Distribution of actual water volume along the width direction in the secondary cooling zone: (a) Seg. 1; (b) Segs. 2 and 3; (c) Segs. 4 and 5; (d) Segs. 6–9.

2.3. Model validation

The nail shooting test is a direct and accurate method to measure the thickness of continuous-cast billets and slabs [32–33]. The nail shooting test is to shoot the nail embedding with sulfur into the high-temperature slabs, and determine the thickness of the shell by observing the morphology of the nail in the slab. Nails will not melt in the solid phase, and sulfur embedded in the nail hardly diffuses. In the two-phase zone and liquid phase zone, the nail will gradually melt, and the sulfur will diffuse around.

In this study, nail shooting method was used to measure the shell thickness at the exit of Seg. 6 at the 1/2, 1/4, and 1/8 positions in slab width. After the nail shooting test, samples with nails were cut from the 1/2, 1/4, and 1/8 width of the slab, and then the samples were machined and pickled. Positions of the unmelted nail heads were highlighted by red lines in Fig. 4. Results of nail shooting test show that the thicknesses of shell at 1/2, 1/4, and 1/8 positions in slab width were 85, 80, and 76 mm, respectively (Fig. 4). The shell thickness difference of the same section was greater than or equal to 9 mm.

As shown in Fig. 5 (a), the simulation results agree well with the nail shooting test findings. Fig. 5(b) displays the comparison between the simulated calculation of temperature distribution along the width direction on the slab surface at the end of Seg. 6 and the measured results by handheld infrared temperature measurement equipment. Given the influence of the measuring environment, the simulated results agree with the actual conditions.

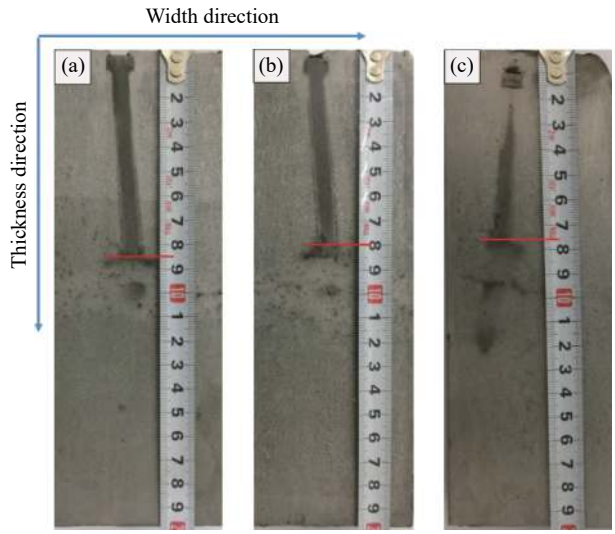

Fig. 4. Results of nail shooting specimens at different locations: (a) 1/2, (b) 1/4, and (c) 1/8 width.

3. Influence of continuous-cast process on shape of solidification end

3.1. Solid fraction profile of slab at different locations

The simulation calculation of slab solidification process

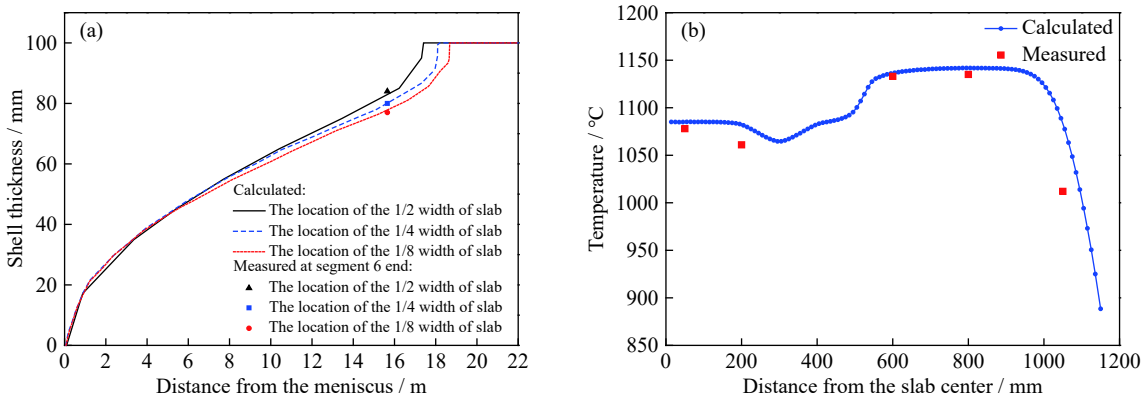

Fig. 5. Comparison of simulation and experimental results: (a) shell thickness; (b) temperature of slab surface.

with superheat of 25°C and at the casting speed of 1.05 m/min was completed. Figs. 6(a) and 6(b) show the solid fraction profile of 1/2 transverse section of the slab at the end of Segs. 6 and 7, respectively. Given the relatively strong cooling in the middle of the slab, the central solid fraction of slab in the 1/2 width location was significantly lower than that in the 1/4–1/8 width location at the end of Seg. 6, as shown in Fig. 6(a). The shape of the solidification end in the slab was complicated, and the final solidification end position was about 220–440 mm away from the edge of the slab, as shown in Fig. 6(b).

3.2. Effect of casting speed on the shape of solidification end

To describe the characteristics of the shape of slab solidification end, we defined the center point of 1/2 width in slab as A and the center point of 1/8 width in slab as B (Fig. 7).

$L_{A,f_s=0.10}$ and $L_{B,f_s=0.10}$ are the distance from points A and B to the meniscus of the mold when the solid fraction at points A and B are 0.10, respectively. $L_{A,f_s=0.90}$ and $L_{B,f_s=0.90}$ are the distance from points A and B to the meniscus of the mold when the solid fraction at points A and B are 0.90, respectively. As shown in Table 3, four parameters were defined to better characterize the shape of the solidification end.

Figs. 8(a), 8(b), and 8(c) show the shapes of the slab solidification end when the casting speeds were 0.95, 1.05, and 1.15 m/min, respectively. The solidification end of slab moved backward when the casting speed increased. When the casting speed increased from 0.95 to 1.05 and 1.15 m/min, the $L_{A,f_s=0.10}$ extended backward by 1.37 and 2.76 m,

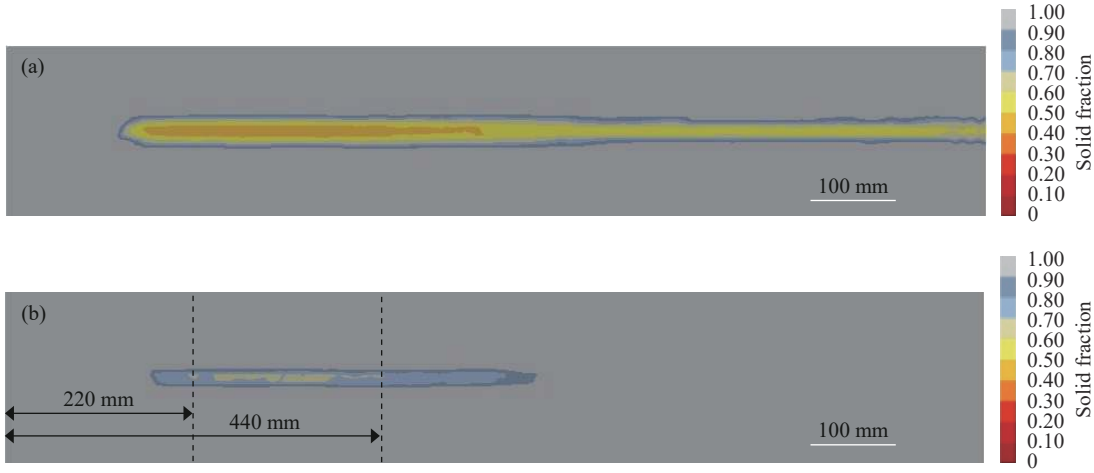

Fig. 6. Calculation results of slab solidification: (a) solid fraction profile at the end of Seg. 6; (b) solid fraction profile at the end of Seg. 7.

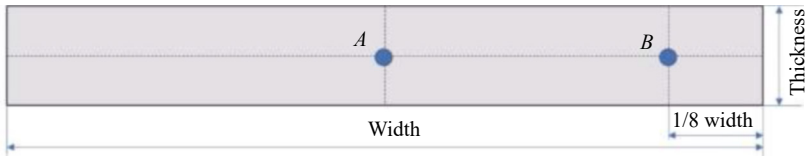

Fig. 7. Position diagram of typical solidification points of slab.

Table 3. Characterization parameters of solidification end morphology

No.	Parameter	Characterization	Computational formula
1	S_{I1}	Nonuniformity at the beginning of solidification	$L_{B,f_s=0.10} - L_{A,f_s=0.10}$
2	S_{I2}	Nonuniformity at the end of solidification	$L_{B,f_s=0.90} - L_{A,f_s=0.90}$
3	S_{I3}	The solidification end length	$L_{B,f_s=0.90} - L_{A,f_s=0.10}$
4	S_{I4}	The solidification unevenness	$(L_{B,f_s=0.90} - L_{A,f_s=0.10}) / (L_{A,f_s=0.90} - L_{A,f_s=0.10})$

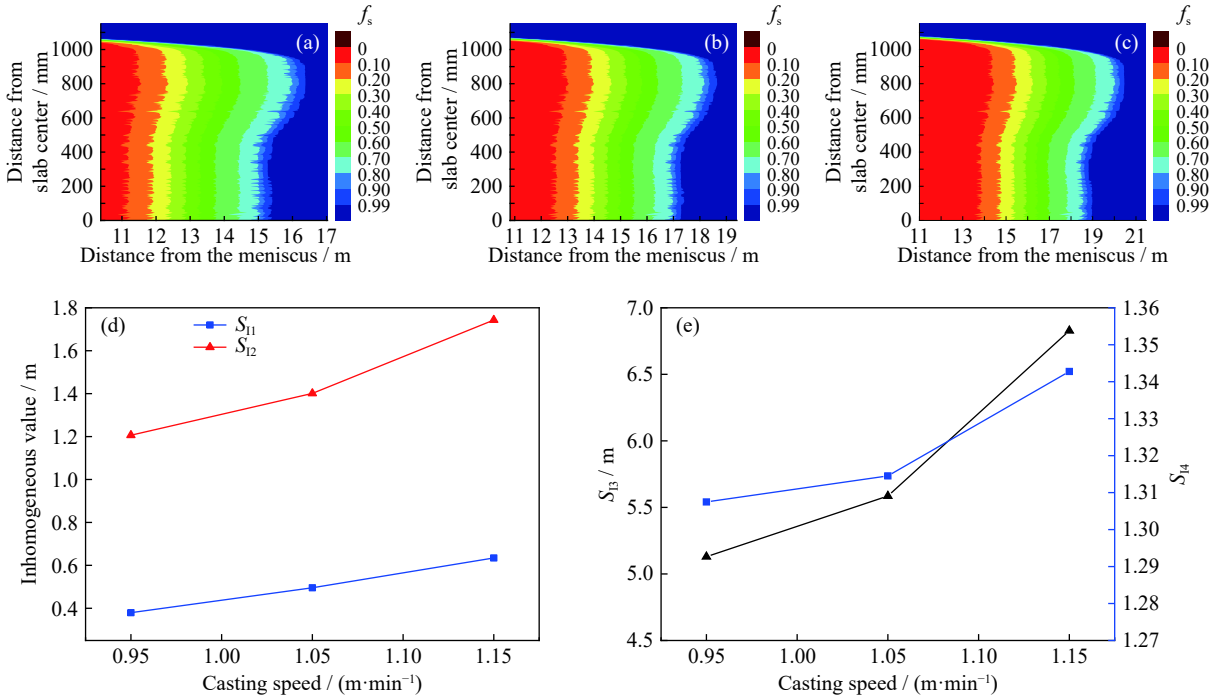

Fig. 8. Effect of different casting speeds on the shape of slab solidification end: (a) shape of solidification end at 0.95 m/min; (b) shape of solidification end at 1.05 m/min; (c) shape of solidification end at 1.15 m/min; (d) trend of S_{I1} and S_{I2} along with the casting speed; (e) trend of S_{I3} and S_{I4} along with the casting speed.

respectively. The $L_{A,f_s=0.90}$ extended backward by 1.90 and 3.92 m under the same conditions. The $L_{B,f_s=0.10}$ extended backward by 1.48 and 3.01 m, and $L_{B,f_s=0.90}$ extended backward by 2.10 and 4.46 m. As shown in Fig. 8(d), the nonuniformity at the beginning and end of solidification (S_{I1} and S_{I2}) increase with the increase in the casting speed. As shown in Fig. 8(e), the solidification end length (S_{I3}) increased from 5.13 m at 0.95 m/min to 6.83 m at 1.15 m/min, and the solidification unevenness (S_{I4}) increased from 1.307 at 0.95 m/min to 1.342 at 1.15 m/min. These findings are mainly due to the fixed heat released by the unit length of the slab during the solidification process under the same composition and superheat conditions. With the increase in casting speed, the time of continuous-cast slab in the mold and the curved section was shortened. The shortened time caused more solidification processes to shift to the non-uniform cooling region, which exacerbated the unevenness of the solidification end.

3.3. Effect of superheat on the shape of solidification end

Figs. 9(a)–9(c) show the shapes of the solidification end during the superheating of molten steel at 10, 25, and 40°C, respectively. When the superheat values were 10, 25, and 40°C, the $L_{A,f_s=0.10}$ were 11.76, 12.32, and 12.85 m, respectively. The values for $L_{A,f_s=0.90}$ reached 16.27 (10°C), 16.77 (25°C), and 17.29 (40°C) m. For each 10°C increase, the $L_{A,f_s=0.10}$ and $L_{A,f_s=0.90}$ extended backward by about 0.36 and 0.34 m, respectively. When the superheat values were 10, 25, and 40°C, the $L_{B,f_s=0.10}$ were 12.18, 12.81, and 13.38 m, respectively. The values for $L_{B,f_s=0.90}$ reached 17.56 (10°C), 18.17 (25°C), and 18.85 (40°C) m. For every 10°C increase, $L_{B,f_s=0.10}$ and $L_{B,f_s=0.90}$ extended backward by about 0.40 and 0.43 m, respectively. As shown in Fig. 9(d), S_{I1} and S_{I2} both increased with the increase in superheat. The S_{I3} increased slightly with the increase in superheat, as shown in Fig. 10(e). However, for each 10°C increase, S_{I4} rose by about 0.022, which indicates that superheat has a significant effect on the solidification unevenness.

3.4. Effect of secondary cooling strength on the shape of solidification end

Figs. 10(a)–10(c) show the shapes of slab solidification end when the relative secondary cooling strengths were 0.8,

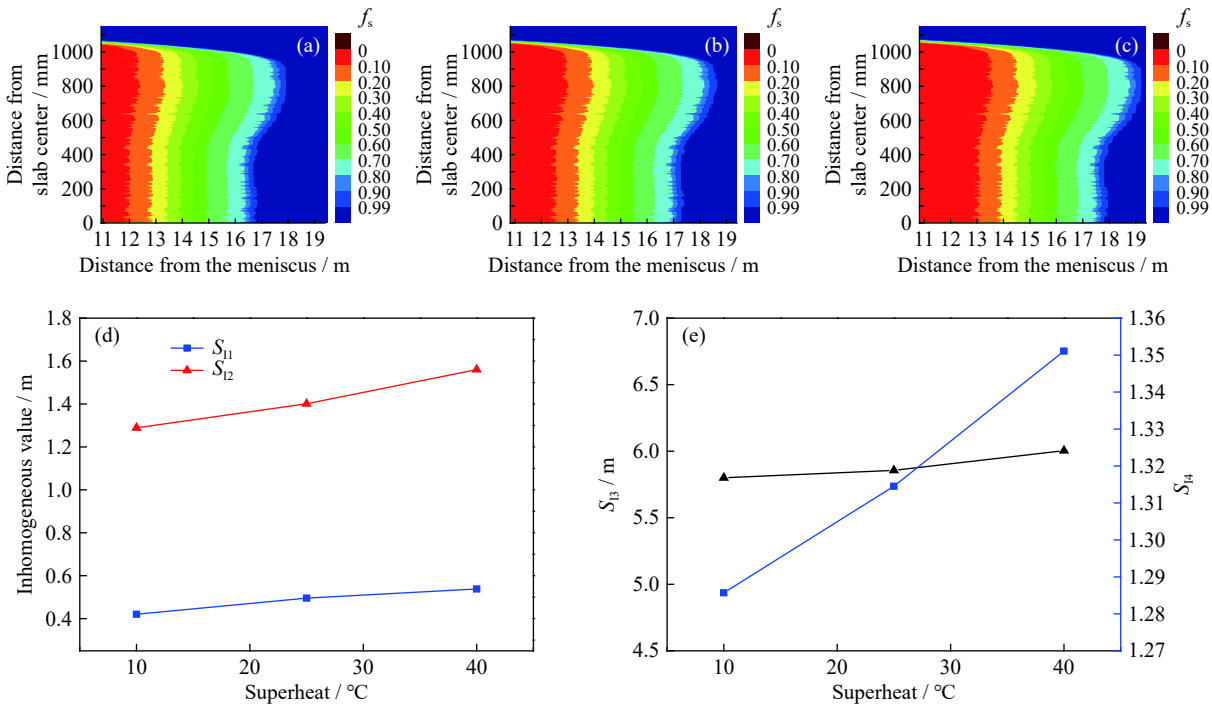

Fig. 9. Effect of superheat on the shape of slab solidification end: (a) shape of slab solidification end with superheat = 10°C; (b) shape of slab solidification end with superheat = 25°C; (c) shape of slab solidification end with superheat = 40°C; (d) trend of S_{I1} and S_{I2} along with superheat; (e) trend of S_{I3} and S_{I4} along with superheat.

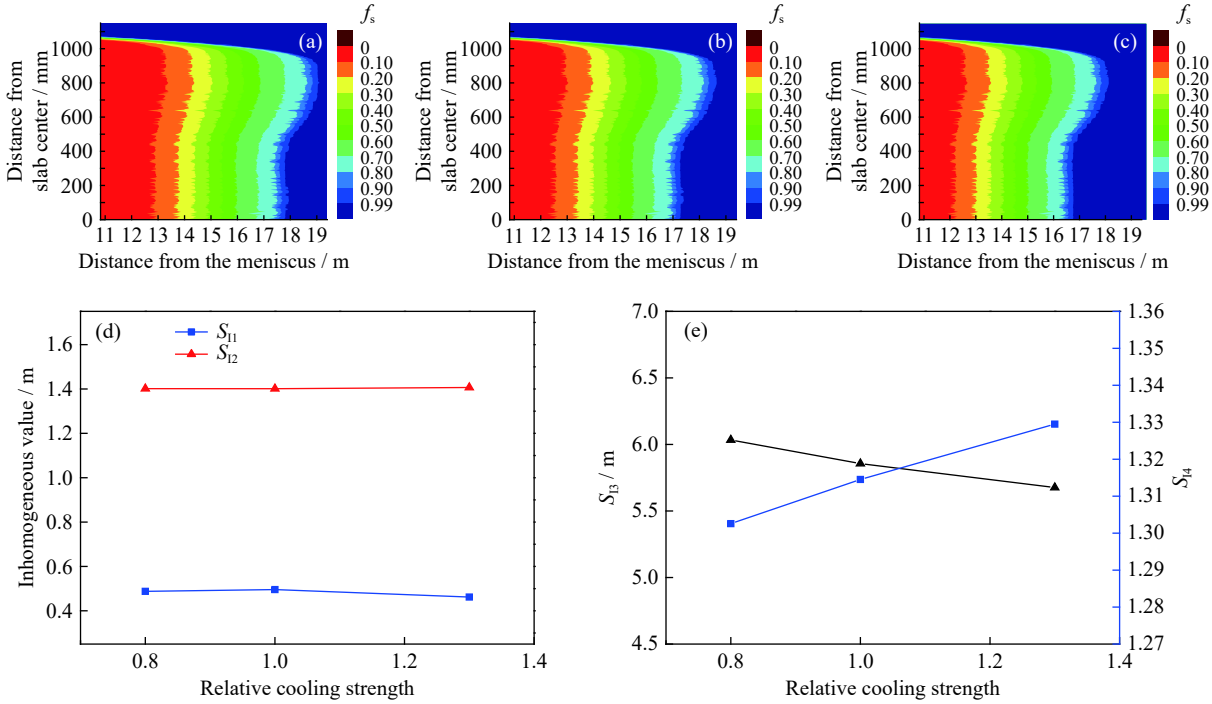

Fig. 10. Effect of secondary cooling strength on the shape of solidification end: (a) relative secondary cooling strength = 0.8; (b) relative secondary cooling strength = 1.0; (c) relative secondary cooling strength = 1.3; (d) trend of S_{I1} and S_{I2} along with the relative cooling strength; (e) trend of S_{I3} and S_{I4} along with the relative cooling strength.

1.0, and 1.3, respectively. At the relative secondary cooling strengths of 0.8, 1.0, and 1.3, the $L_{A,f_s=0.10}$ were 12.65, 12.32, and 11.97 m, respectively. The values for $L_{A,f_s=0.90}$ reached 17.28 (0.8), 16.77 (1.0), and 16.24 (1.3) m. When the relative secondary cooling strengths were 0.8, 1.0, and 1.3, the $L_{B,f_s=0.10}$ amounted to 13.14, 12.81, and 12.44 m, respectively. The

values for $L_{B,f_s=0.90}$ respectively totaled 18.68, 18.17, and 17.65 m under the same cooling strengths. As shown in Fig. 10(d), S_{I1} decreased a bit with the increase in the secondary cooling strength. S_{I2} hardly changed with the increase in secondary cooling strength. As shown in Fig. 10(e), S_{I3} decreased along with the rise in secondary cooling strength, whereas S_{I4} increased along with the increase in cooling strength.

The effect of MSR improved for a small solidification end inhomogeneous value. However, ideal homogeneous solidification is almost nonexistent. The process needs to be adjusted to achieve relatively optimal results.

4. Effect of nonuniform cooling on central segregation

Four different processes were investigated to study the effect of MSR on the central segregation of non-uniform solidification slab. The chemical compositions of steels in the investigation are given in Table 4, and the casting conditions for the tests are presented in Table 5.

A cross-sectional slab slice was cut for each case, and two samples, S1 and S2, were taken from each slab slice. The schematic illustration of the sampling is shown in Fig. 11, and the specific sampling positions of those two samples can be found in it. Acid tests were carried out on the samples after polishing to observe the central segregation of the slab.

Table 4. Chemical compositions of steels in the investigation

wt%

Steel	C	Si	Mn	P	S	Fe
Case 1	0.18	0.22	1.25	0.007	0.0024	Bal.
Case 2	0.16	0.29	1.25	0.015	0.0014	Bal.
Case 3	0.19	0.27	1.32	0.011	0.0017	Bal.
Case 4	0.17	0.27	1.30	0.013	0.0010	Bal.

Table 5. Casting conditions for tests

Steel	Casting speed / (m·min^{-1})	Secondary cooling strength / (L·kg^{-1})	Actual reduction / mm		Superheat / °C
			Seg. 6	Seg. 7	
Case 1	1.05	0.35	2.00	2.00	26
Case 2	1.05	0.43	2.00	2.00	26
Case 3	1.05	0.49	2.00	2.00	23
Case 4	1.05	0.35	0	0	19

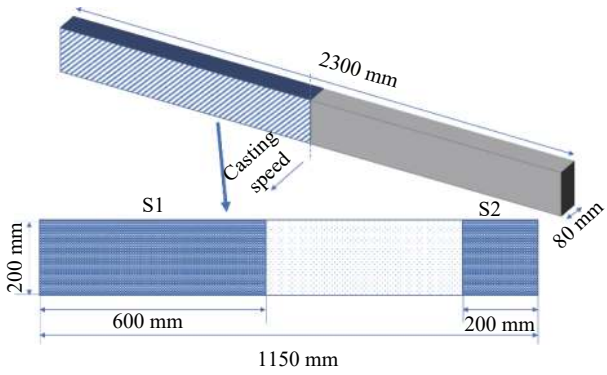

Fig. 11. Schematic illustration of continuous-cast slab sampling for each case.

Fig. 12 shows the morphology of central segregation in the main position of continuous-cast slab under four different process conditions.

Case 1-S1 and Case 4-S1 show no evident central segregation within 364 and 124 mm from the slab edge, respectively. The central segregation of Case 4-S2 was more serious than that of Case 1-S2. The results show that with the same casting speed and cooling strength, the center line within the range of 124–364 mm originated from the narrow edge of the slab. The 1/2 width of the slab was notably improved by the implementation of the MSR process.

Cases 1, 2, and 3 had the same casting speed, MSR rate, and cooling system of the mold, and the only difference was the secondary cooling strength. As shown in Figs. 12(a), 12(c), and 12(e), a remarkable central segregation appeared at the positions of 364, 287.5, and 136 mm away from the narrow edge, respectively. In these cases, the most serious segregation area was around the 1/4 width (575 mm from the slab edge), whereas a relatively slight central segregation occurred near the 1/2 width, as shown in Figs. 12(b), 12(d), and 12(f).

Fig. 13 shows the MSR range of the typical position of a slab with three different secondary cooling processes. In the three cases, MSR was carried out in the two-phase region. However, at the same position, evident differences were observed in the central solid fraction of different processes, which should be the main reason for the differences in the morphology of the central segregation of different slabs.

The smaller the S_{I3} is, the smaller the length of solidification end is, which benefits MSR. However, the S_{I3} of Case 3 was the smallest, and the corresponding slab center segregation is not the best. This finding is mainly due to the unsuitability of the MSR zone. From the results, if the 1/4 width position of slab is the representative point, then the best MSR zone is f_s = 0.19 to 0.71.

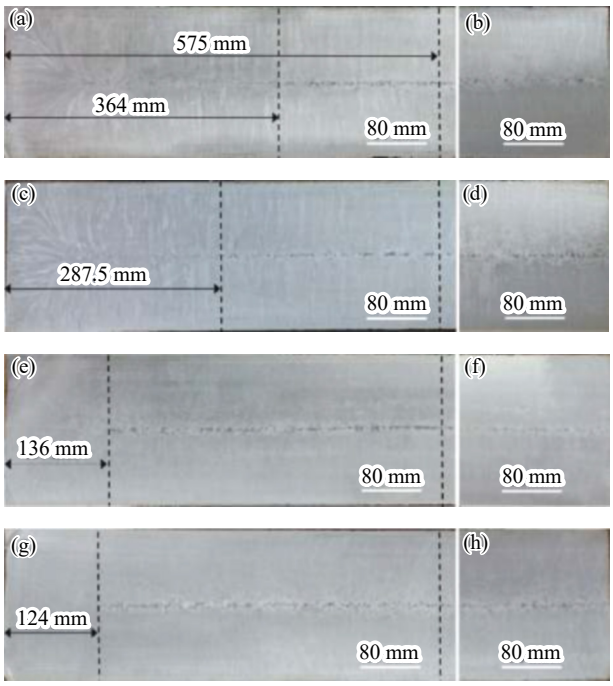

Fig. 12. Macrostructure of slab with different MSR processes: (a) Case 1-S1; (b) Case 1-S2; (c) Case 2-S1; (d) Case 2-S2; (e) Case 3-S1; (f) Case 3-S2; (g) Case 4-S1; (h) Case 4-S2.

The difference in central segregation near the 1/8 width of the slab was due to the flow of molten steel enriched with solute elements under MSR. In the mushy area, the velocity of liquid steel (v_x) can be estimated by Darcy's law:

$$v_x = -\frac{K}{\mu g_L}\frac{dP}{dx} \tag{8}$$

where K is permeability, m^2; dP/dx is pressure gradient, Pa/m; μ is viscosity, Pa·s; g_L is liquid fraction.

The permeability of isotropic porous medium is typically described by using the Kozeny–Carman equation [34]:

$$K = \frac{1}{kS_v}\frac{g_L^3}{(1-g_L)^2} \tag{9}$$

where k is Kozeny constant, and S_v is the solid/liquid surface in unit volume, m^2.

From Eqs. (8) and (9), the velocity of liquid steel can be expressed as follows:

$$v_x = -\frac{g_L^2}{k\mu S_v(1-g_L)^2}\frac{dP}{dx} \tag{10}$$

In the case of MSR, the increase in external force increases the flow velocity, especially in the region with a high liquid ratio. Case 1 was considered an example to explain the effect of MSR on the central segregation of non-uniform solidification slab. The solid fraction profile of case 1 at the end of Seg. 6 is shown in Fig. 14. At the end of Seg. 6, the slab has completely solidified in the area 115 mm from the narrow edge, and MSR has little effect on the central segregation morphology in this area.

The central solid fraction of 1/2 width was in the range of 0.40 to 0.50, but the central solid fractions at 1/4 to 1/8 width were still in the range of 0.20 to 0.30 at the end of Seg. 6 (Fig. 14). A large solid fraction difference was observed in the width. The flow direction of molten steel was from 1/8 width position to 1/2 width position. Under the same hydrostatic pressure and external force (mainly the MSR force), the flow rate of liquid core is related to viscosity and solid phase rate. The higher the solid fraction, the lower the flow rate. Therefore, the transverse flow of the central segregation near the 1/2 width was small. Given that the flow rate of liquid steel was the highest near the 1/8 width, when it flowed to the position of 1/4 width, a longitudinal fresh liquid steel filled

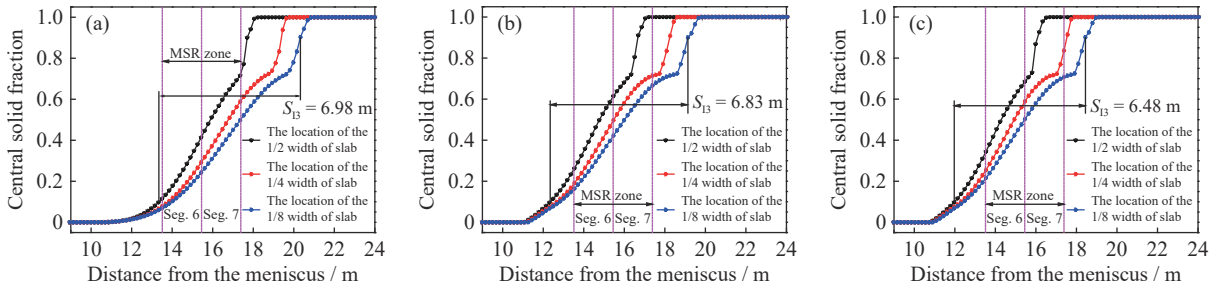

Fig. 13. Central solid fraction at the start and end of MSR at typical locations and the S_{I3} under different cooling strengths: (a) 0.35 L/kg; (b) 0.43 L/kg; (c) 0.49 L/kg.

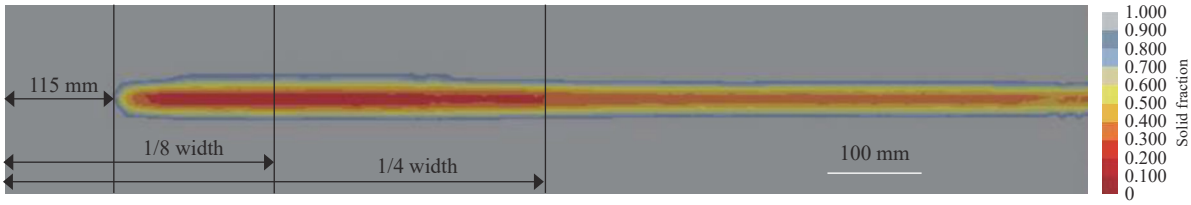

Fig. 14. Solid fraction profile at the end of Seg. 6.

the gap, relieving the central segregation.

The test results show that there will be transverse flow in the uneven slab liquid core with the pressure of MSR when the central solid fraction of the slab is lower than 0.20. Although the location central segregation can be reduced, the flowing molten steel with solute enrichment will lead to the segregation gathering at other positions.

5. Conclusions

The current study developed a solidification model to explore the effects of casting speed, superheat, and secondary cooling intensity on the shape of solidification end for a wide continuous-cast slab. Moreover, central segregation of slabs with different processes was investigated. The conclusions can be summarized as below.

(1) The casting speed showed a considerable effect on the shape of solidification end. With the increase in casting speed, additional slab solidification occurred in the non-uniform cooling zone. The nonuniformity at the beginning and end of solidification, the solidification end length, and the solidification unevenness increased with the increase in casting speed.

(2) The increase in superheat led to an increased nonuniformity at the beginning and end of solidification. The superheat had the greatest influence on the solidification unevenness. For each 10°C increase, the solidification unevenness increased by about 0.022. However, the superheat showed negligible effects on the solidification end length.

(3) The secondary cooling strength resulted in a complex effect on the solidification end shape of the slab. The secondary cooling strength showed minimal effect on the nonuniformity at the beginning and end of solidification. With the increase in secondary cooling intensity, the solidification end length decreased. Meanwhile, the inhomogeneity of transverse cooling increased, which caused the increase in solidification unevenness.

(4) With the MSR, the morphology of central segregation formed at different shape of solidification end notably differed. When the solid fraction was less than 0.20, the transverse flow of liquid steel influenced the morphology of the central segregation.

Acknowledgements

This research was financially supported by the National Natural Science Foundation of China (Nos. 51774030 and U1860104) and the Fundamental Research Funds for the Central Universities, China (No. N2025019).

References

[1] M.C. Flemings, Our understanding of macrosegregation: Past and present, *ISIJ Int.*, 40(2000), No. 9, p. 833.

[2] Z. Chen and H.F. Shen, Simulation of macrosegregation in a 36-t steel ingot using a multiphase model, *Int. J. Miner. Metall. Mater.*, 27(2020), No. 2, p. 200.

[3] X.G. Zhang, K. Matsuura, and M. Ohno, Abnormal grain growth in austenite structure reversely transformed from ferrite/pearlite-banded structure, *Metall. Mater. Trans. A*, 45(2014), No. 10, p. 4623.

[4] T.F. Majka, D.K. Matlock, and G. Krauss, Development of microstructural banding in low-alloy steel with simulated Mn segregation, *Metall. Mater. Trans. A*, 33(2002), No. 6, p. 1627.

[5] G. Krauss, Solidification, segregation, and banding in carbon and alloy steels, *Metall. Mater. Trans. B*, 34(2003), No. 6, p. 781.

[6] Y.S. Han, W. Yan, J.S. Zhang, W.Q. Chen, J. Chen, and Q. Liu, Optimization of thermal soft reduction on continuous-casting billet, *ISIJ Int.*, 60(2020), No. 1, p. 106.

[7] Y. Chen, M.F. Xiao, and G.R. Wu, Dynamic soft reduction technology for bloom casting, *J. Iron Steel Res. Int.*, 17(2010), No. 6, p. 1.

[8] Z.W. Han, D.F. Chen, K. Feng, and M.J. Long, Development and application of dynamic soft-reduction control model to slab continuous casting process, *ISIJ Int.*, 50(2010), No. 11, p. 1637.

[9] M. Vynnycky, Applied mathematical modelling of continuous casting processes: A review, *Metals*, 8(2018), No. 11, art. No. 928.

[10] J. Zeng, W.Q. Chen, Q.X. Wang, and G.S. Wang, Improving inner quality in continuous casting rectangular billets: Comparison between mechanical soft reduction and final electromagnetic stirring, *Trans. Indian Inst. Met.*, 69(2016), No. 8, p. 1623.

[11] A.N. Zavalishchin, M.I. Rumyantsev, D.N. Chikishev, M.V. Efremova, and E.V. Kozhevnikova, Influence of "soft" reduction on the structure of continuous cast ingot and the properties of rolled products of microalloyed steels, *Metallurgist*, 63(2019), No. 3-4, p. 238.

[12] L. Li, X. Zhao, P. Lan, Z.P. Tie, H.Y. Tang, and J.Q. Zhang, Effect of roll surface profile on thermal-mechanical behavior of continuously cast bloom in soft reduction process, [in] *TMS 2019 148th Annual Meeting & Exhibition Supplemental Proceedings*, Springer, Cham, 2019, p. 93.

[13] R. Thome and K. Harste, Principles of billet soft-reduction and consequences for continuous casting, *ISIJ Int.*, 46(2006), No. 12, p. 1839.

[14] C.H. Yim, J.K. Park, B.D. You, and S.M. Yang, The effect of soft reduction on center segregation in C.C. slab, *ISIJ Int.*, 36(1996), No. Suppl, p. S231.

[15] M. Jauhola and M. Haapala, The latest results of dynamic soft reduction in slab CC-machine, [in] *83rd Steelmaking Conference Proceedings*, Pittsburgh, 2000, p. 201.

[16] C. Ji, S. Luo, M.Y. Zhu, and Y. Sahai, Uneven solidification during wide-thick slab continuous casting process and its influence on soft reduction zone, *ISIJ Int.*, 54(2014), No. 1, p. 103.

[17] Y. Ito, A. Yamanaka, and T. Watanabe, Internal reduction efficiency of continuously cast strand with liquid core, *Rev. Met. Paris*, 97(2000), No. 10, p. 1171.

[18] M.H. Wu, J. Domitner, and A. Ludwig, Using a two-phase columnar solidification model to study the principle of mechanical soft reduction in slab casting, *Metall. Mater. Trans. A*, 43(2012), No. 3, p. 945.

[19] J. Domitner, M.H. Wu, A. Kharicha, A. Ludwig, B. Kaufmann, J. Reiter, and T. Schaden, Modeling the effects of strand surface bulging and mechanical softreduction on the macrosegregation formation in steel continuous casting, *Metall. Mater.*

Trans. A, 45(2014), No. 3, p. 1415.
[20] B. Rogberg and L. Ek, Influence of soft reduction on the fluid flow, porosity and center segregation in CC high carbon- and stainless steel blooms, *ISIJ Int.*, 58(2018), No. 3, p. 478.
[21] Z.Z. Cai and M.Y. Zhu, Non-uniform heat transfer behavior during shell solidification in a wide and thick slab continuous casting mold, *Int. J. Miner. Metall. Mater.*, 21(2014), No. 3, p. 240.
[22] D.P. Li, H.Z. Wu, H.F. Wang, and H. Li, Growth of solidified shell in bloom continuous casting mold of hypo-peritectic steel based on a FeS tracer method, *J. Iron Steel Res. Int.*, 27(2020), No. 7, p. 782.
[23] M.J. Long, Z.H. Dong, D.F. Chen, Q. Liao, and Y.G. Ma, Effect of uneven solidification on the quality of continuous casting slab, *Int. J. Mater. Prod. Technol.*, 47(2013), No. 1/2/3/4, p. 216.
[24] H. Preßlinger, S. Ilie, P. Reisinger, A. Schiefermüller, A. Pissenberger, E. Parteder, and C. Bernhard, Methods for assessment of slab centre segregation as a tool to control slab continuous casting with soft reduction, *ISIJ Int.*, 46(2006), No. 12, p. 1845.
[25] S.K. Choudhary, S. Ganguly, A. Sengupta, and V. Sharma, Solidification morphology and segregation in continuously cast steel slab, *J. Mater. Process. Technol.*, 243(2017), p. 312.
[26] P. Fei, Y. Min, C.J. Liu, and M.F. Jiang, Effect of continuous casting speed on mold surface flow and the related near-surface distribution of non-metallic inclusions, *Int. J. Miner. Metall. Mater.*, 26(2019), No. 2, p. 186.
[27] J. Savage and W.H. Pritchard, The problem of rupture of the billet in the continuous casting of steel, *J. Iron Steel Inst.*, 178(1954), No. 3.
[28] S. Louhenkilpi, J. Miettinen, and L. Holappa, Simulation of microstructure of as-cast steels in continuous casting, *ISIJ Int.*, 46(2006), No. 6, p. 914.
[29] T. Nozaki, J.I. Matsuno, K. Murata, H. Ooi, and M. Kodama, A secondary cooling pattern for preventing surface cracks of continuous casting slab, *Trans. Iron Steel Inst. Jpn.*, 18(1978), No. 6, p. 330.
[30] J.S. Ha, J.R. Cho, B.Y. Lee, and M.Y. Ha, Numerical analysis of secondary cooling and bulging in the continuous casting of slabs, *J. Mater. Process. Technol.*, 113(2001), No. 1-3, p. 257.
[31] R.A. Hardin, K. Liu, C. Beckermann, and A. Kapoor, A transient simulation and dynamic spray cooling control model for continuous steel casting, *Metall. Mater. Trans. B*, 34(2003), No. 3, p. 297.
[32] M.J. Long, D.F. Chen, Q.X. Wang, D.H. Luo, Z.W. Han, Q. Liu, and W.X. Gao, Determination of CC slab solidification using nail shooting technique, *Ironmaking Steelmaking*, 39(2012), No. 5, p. 370.
[33] C. Ji, S. Luo, and M.Y. Zhu, Analysis and application of soft reduction amount for bloom continuous casting process, *ISIJ Int.*, 54(2014), No. 3, p. 504.
[34] M. Réger, B. Verő, R. Józsa, and Z. Csepeli, Effect of mushy zone permeability on the formation of centerline segregation in slab casting, *Mater. Sci. Forum*, 790-791(2014), p. 296.